EBioMedicine 67 (2021) 103381

Contents lists available at ScienceDirect

EBioMedicine

journal homepage: www.elsevier.com/locate/ebiom

Q493K and Q498H substitutions in Spike promote adaptation of SARS-CoV-2 in mice

Kun Huang[a,b,c,#], Yufei Zhang[a,b,c,#], Xianfeng Hui[a,b,c], Ya Zhao[a,b,c], Wenxiao Gong[a,b,c], Ting Wang[a,b,c], Shaoran Zhang[a], Yong Yang[a,b,c], Fei Deng[d], Qiang Zhang[a,b,c], Xi Chen[b], Ying Yang[a,b,c], Xiaomei Sun[a,b,c], Huanchun Chen[a,b], Yizhi J. Tao[e], Zhong Zou[a,b,c,*], Meilin Jin[a,b,c,*]

[a] State Key Laboratory of Agricultural Microbiology, Huazhong Agricultural University, Wuhan 430070, PR China
[b] College of Veterinary Medicine, Huazhong Agricultural University, Wuhan, 430070, PR China
[c] Key Laboratory of development of veterinary diagnostic products, Ministry of Agriculture, Wuhan, 430070, PR China
[d] State Key Laboratory of Virology and National Virus Resource Center, Wuhan Institute of Virology, Chinese Academy of Sciences, Wuhan, 430071, PR China
[e] Department of BioSciences, Rice University, Houston, TX 77005, USA

ARTICLE INFO

Article History:
Received 9 February 2021
Revised 16 April 2021
Accepted 19 April 2021
Available online xxx

Keywords:
SARS-CoV-2
Angiotensin-converting enzyme 2
Mouse-adapted strain
Adaptive mutations
TLR7/8 agonist

ABSTRACT

Background: An ideal animal model to study SARS-coronavirus 2 (SARS-CoV-2) pathogenesis and evaluate therapies and vaccines should reproduce SARS-CoV-2 infection and recapitulate lung disease like those seen in humans. The angiotensin-converting enzyme 2 (ACE2) is a functional receptor for SARS-CoV-2, but mice are resistant to the infection because their ACE2 is incompatible with the receptor-binding domain (RBD) of the SARS-CoV-2 spike protein .

Methods: SARS-CoV-2 was passaged in BALB/c mice to obtain mouse-adapted virus strain. Complete genome deep sequencing of different generations of viruses was performed to characterize the dynamics of the adaptive mutations in SARS-CoV-2. Indirect immunofluorescence analysis and Biolayer interferometry experiments determined the binding affinity of mouse-adapted SARS-CoV-2 WBP-1 RBD to mouse ACE2 and human ACE2. Finally, we tested whether TLR7/8 agonist Resiquimod (R848) could also inhibit the replication of WBP-1 in the mouse model.

Findings: The mouse-adapted strain WBP-1 showed increased infectivity in BALB/c mice and led to severe interstitial pneumonia. We characterized the dynamics of the adaptive mutations in SARS-CoV-2 and demonstrated that Q493K and Q498H in RBD significantly increased its binding affinity towards mouse ACE2. Additionally, the study tentatively found that the TLR7/8 agonist Resiquimod was able to protect mice against WBP-1 challenge. Therefore, this mouse-adapted strain is a useful tool to investigate COVID-19 and develop new therapies.

Interpretation: We found for the first time that the Q493K and Q498H mutations in the RBD of WBP-1 enhanced its interactive affinities with mACE2. The mouse-adapted SARS-CoV-2 provides a valuable tool for the evaluation of novel antiviral and vaccine strategies. This study also tentatively verified the antiviral activity of TLR7/8 agonist Resiquimod against SARS-CoV-2 in *vitro* and in *vivo*.

Funding: This research was funded by the National Key Research and Development Program of China (2020YFC0845600) and Emergency Science and Technology Project of Hubei Province (2020FCA046) and Robert A. Welch Foundation (C-1565).

1. Introduction

Coronavirus disease 2019 (COVID-19) is a fatal respiratory illness that first appeared in Wuhan, China in December 2019 [1]. It is caused by a novel *Betacoronavirus* called severe acute respiratory syndrome coronavirus 2 (SARS-CoV-2). As of November 24 2020, the World Health Organization (WHO) has reported approximately 59 million laboratory-confirmed cases of COVID-19 worldwide, including 1.39 million associated deaths. COVID-19 is characterized by fever, cough, and dyspnea that may progress rapidly to respiratory and cardiac failure requiring mechanical ventilation [2]. Vaccines and antiviral agents are urgently needed to control the pandemic. As of 18 February 2021, at least seven different vaccines across three platforms have been rolled out in different countries. At the same time,

* Corresponding authors.
E-mail addresses: zz19841024@126.com (Z. Zou), jml8328@126.com (M. Jin).
# These authors contributed equally to this work.

https://doi.org/10.1016/j.ebiom.2021.103381

Research in context

Evidence before this study

Mouse-adapted SARS-CoV-2 has been found to contain mutations at several locations in the genome. However, the underlying mechanism explaining the association of these mutations with mouse adaptation is still largely unknown. Moreover, antiviral agents are currently tested in clinical trials as effective treatments are urgently needed to control the pandemic.

Added value of this study

We characterized the dynamics of the adaptive mutations in SARS-CoV-2 and demonstrated that Q493K and Q498H in RBD significantly increased its binding affinity towards mouse ACE2. Additionally, we verified the antiviral activity of Resiquimod against SARS-CoV-2 *in vitro* and *in vivo*, demonstrating this mouse-adapted strain is a useful tool to investigate COVID-19 and develop new therapies.

Implications of all the available evidence

Our dynamic mutation analysis allowed us to dissect the intricate evolutionary processes of SARS-CoV-2 in an unnatural host. These findings suggest that R848 stimulating the response of the body's immune system to SARS-CoV-2 infection alleviate some of the more severe symptoms and reduce mortality from this virus. It may be suitable for prophylaxis or early treatment before patients develop severe clinical symptoms.

more than 200 additional vaccine candidates are in development (https://www.who.int/emergencies/diseases/novel-coronavirus-2019/covid-19-vaccines). In addition, The FDA approved the first treatment for COVID-19, the antiviral drug Remdesivir. Some other investigational drugs are already in clinical trials (https://www.fda.gov/consumers/consumer-updates/know-your-treatment-options-covid-19).

Animal models are highly valuable for the study of viral diseases as they allow detailed investigation of viral pathogenesis and evaluation of antiviral therapies and vaccines. An ideal animal model should not only be permissive to the viral infection, but also be able to develop disease and pathology similar those observed in humans. Clinical signs, viral replication, and pathology are species-dependent when SARS-CoV-2 is delivered into the respiratory tracts of mice, hamsters, ferrets, cats, and nonhuman primates [3–9]. However, the high cost, limited availability, and individual variations associated with these animal models imply that the current systems do not allow sufficient sample size that is required for large-scale studies and statistical evaluation in order to draw robust conclusions.

Shortly after the identification of SARS-CoV-2, it was discovered that this virus uses the human angiotensin-converting enzyme 2 (hACE2) to gain entry into host cells [10], but it is incapable of using the murine ortholog mACE2 as a receptor. In order to develop mouse models for SARS-CoV-2 infection, several strategies have been used to overcome this receptor incompatibility, including the development of transgenic mouse lines expressing hACE2 using exogenous or murine promoters, or transducing animals for hACE2 expression using adenovirus or adeno-associated virus vectors [11,12]. Such transgenic mice have been used previously to study SARS-CoV-2 infection and pathogenesis and to evaluate countermeasures against COVID-19. In addition, mouse adaptation has been successfully used to generate several SARS-CoV-2 strains with enhanced virulence and capable of recapitulating severe SARS-CoV-2 lung disease in mice [13–15]. Mouse-adapted SARS-CoV-2 has been found to contain mutations at several locations in the genome. However, the underlying mechanism explaining the association of these mutations with mouse adaptation is still largely unknown.

In this study, we identified a mouse-adapted SARS-CoV-2 strain (WBP-1) that can productively replicate in the respiratory tract and cause severe interstitial pneumonia in wild-type BALB/c mice. More importantly, we found for the first time that the Q493K and Q498H mutations in the RBD of WBP-1 enhanced its interactive affinities with mACE2, suggesting that WBP-1 is capable of using mACE2 to gain access to the host cells. Additionally, therapeutic treatments including the TLR7/8 agonist Resiquimod (R848) protected the mice against lethal WBP-1 challenge. Therefore, our results demonstrated that WBP-1 and BALB/c mice are a valuable model for the development and testing of SARS-CoV-2 vaccines and therapeutics.

2. Methods

2.1. Viruses, cells, and plaque assays

SARS-CoV-2 strain Wuhan-Hu-1 (NC_045512) was obtained from the Wuhan Institute of Virology, Chinese Academy of Sciences. Strain WBP-1 (EPI_ISL_1615558) was developed in this study. Vero cells and Caco2 cells were cultured in Dulbecco's modified Eagle's medium (DMEM; Hyclone, Logan, UT, USA) supplemented with 10% fetal bovine serum (PAN Biotech, Germany), 100 U/mL penicillin-streptomycin (Thermo Fisher Scientific, Inc.). Cells were incubated at 37 °C in 5% CO2. The SARS-CoV-2 virus stocks were prepared on Vero cells and viral titers were determined by plaque assays. All experiments involving live viruses were performed in a biosafety level 3 (BSL3) facility in the Huazhong Agricultural University.

2.2. Ethics statement

Female 12-month- or 4-6-week-old BALB/c mice were used for the experiments. Mice were purchased from the Center for Animal Disease Control, Hubei Province. The animal experiments were approved by the Research Ethics Committee, Huazhong Agricultural University, Hubei, China (HZAUMO-2020-0007). All the animal experiments were conducted in accordance with the recommendations in the Guide for the Care and Use of Laboratory Animals from the Research Ethics Committee, Huazhong Agricultural University, Hubei, China.

2.3. Serial passage of SARS-CoV-2 in mice

A dose of 2.3×10^5 plaque forming unit (PFU) of SARS-CoV-2 (Wuhan-Hu-1) was administered intranasally to three anesthetized, female 12-month-old BALB/c mice in 50 μL DMEM. Three days after inoculation, mice were euthanized and their lungs were collected and homogenized with the Tissue Cell-Destroyer (D1000, Novastar, China) in 1 mL DMEM supplemented with antibiotics (100 U/mL penicillin-streptomycin). The lung homogenate was clarified through high-speed centrifugation at 12,000 rpm for 5 min. The mixed supernatant, named mice adaptive passage 1 (P1), was administered intranasally to three female 4–6-week-old BALB/c mice. The process of intranasal inoculation of three female 4–6-week-old mice with viruses collected three days post infection (dpi) was repeated 10 times to obtain mouse-adapted virus strain that cause respiratory disease in mice.

2.4. Virus lethal phenotype identification

At every three passages (P2, P5, P8, and P11), 50 μL of lung homogenate was used for intranasal infection of six female 4–6-week-old mice randomly. Three mice were sacrificed at 3 dpi to harvest lungs. For pathogenicity analysis, each lung was split in half. The right half was collected in 1 mL of RNA later (Ambion, TX, USA) for

viral RNA load analysis and the other half was placed in formalin for histopathologic analysis. Three remaining mice were observed daily for 7 dpi for signs of disease and death to identify the lethal phenotype of mouse-adapted SARS-CoV-2. Clonal isolates of the WBP-1 virus were obtained through plaque purification. Confluent Vero cells were incubated with 10-fold serial dilutions of P11 lung homogenate at 37 °C for 1 h. The cells were washed and overlaid with 1% agarose gel in virus culture medium. After two days, plaques were picked using sterile pipette tips and used to infect Vero cells. Five clones were obtained through three rounds of plaque purification. We chosed the most pathogenic strain and named it WBP-1.

2.5. Complete genome deep sequencing

Complete genome deep sequencing of different generations of viruses was performed to examine the underlying processes and dynamics of viral growth in mice. The P2, P5, P8, and P11 viral RNA pools were extracted from the supernatant of virus-infected lung homogenates using the QIAamp viral RNA mini kit (Qiagen, Hilden, Germany) according to the manufacturer's protocol. These viral RNA pools, together with mouse-adapted WBP-1 and WT Wuhan-Hu-1 viral RNA samples, were sent to Frasergen (Wuhan Frasergen Bioinformatics Co., Ltd., Wuhan, China) for library preparation and sequencing. Virus genome copies were quantified from each sample through quantitative reverse transcription PCR (RT-qPCR) targeting the N gene of SARS-CoV-2 according to instructions provided (Shanghai GeneoDX Biotech CO., Ltd).After removal of host contamination from raw reads, the sequencing data required the KneadData pipeline (https://bitbucket.org/biobakery/kneaddata) for quality control and the polymorphism analysis were generated using alignment-based tool Bowtie 2 [v2.3.5] [16]. The BAM files obtained were used as input on LoFreq [v2.1.2] for the detection of mutations [17]. All reads were mapped to SARS-CoV-2 reference genome (Wuhan-Hu-1, GenBank accession number MN908947).

2.6. Virulence of WBP-1 virus in mice

Virulence was measured as the lethal dose in 4–6-week-old female mice. The lethal dose (LD_{50}) was measured by intranasal infection of four randomly assigned groups of five mice, each receiving 10-fold serial dilutions containing 10^2 to 10^5 PFU of the WBP-1 virus in 50 μL DMEM. Mice in the control group were mock-infected with DMEM. Body weight and survival were monitored daily for 10 days. All mice showing more than 20% body weight loss and respiratory distress were humanely euthanized. LD_{50} was calculated with the Karber method as described by Hawkes [18].

To further characterize mouse-adapted SARS-CoV-2 WBP-1, six randomly selected mice were intranasally infected with 2 LD_{50} of WBP-1 virus; mice in the control group were mock-infected with DMEM. Mice were euthanized at 3 and 5 dpi. Organs were split in half for further studies. For lungs, the right half was collected in 1 mL PBS supplemented with antibiotics (100 U/mL penicillin-streptomycin) and the left was placed in formalin for histopathology and immunohistochemistry. Viral RNA copies in organs (heart, liver, lung, kidney, brain, intestine, trachea, turbinate, and spleen) and cytokine mRNA levels in lung were determined through qRT-PCR (Table S2). Infectious virions in the lung were determined through plaque assays.

2.7. Histopathology and immunohistochemistry

Organs obtained from individual mice euthanized at various time points were fixed in 10% neutral buffered formalin for 7 days. Sections (4 μm thick) were stained with hematoxylin and eosin (H&E) and examined through light microscopy. For immunohistochemistry, fixed tissues were paraffin-embedded, sectioned, and stained with rabbit-anti ACE2 (Abcam, ab108252, 1:200), SARS-CoV-2 nucleocapsid antibody (Sino Biological, China, 40588-R001, 1:200). Goat anti-rabbit immunoglobulin conjugated to peroxidase (Maxim Bio, Fujian, China) was used as secondary antibody. Screening of sections was performed with an Olympus BX51 microscope coupled to a camera.

2.8. SARS-CoV-2 S RBD and ACE2 analysis and modeling

The crystal structure of SARS-CoV-2 RBD and hACE2 is publicly available and contact residues were previously identified. The binding mode between RBD and ACE2 was performed by rigid body docking program ZDOCK and integrated in Discovery Studio (Accelrys Software Inc.). Accession numbers used were SARS-CoV-2 Wuhan-Hu-1 (NC_045512), human ACE2 (AB046569) and mouse ACE2 (NM_001130513).

2.9. Indirect immunofluorescence analysis

Human (hACE2) and mouse (mACE2) ACE2 were cloned into p3XFLAG with NotI/XbaI and XbaI/BglII, respectively, and verified by sequencing. Purified p3XFLAG or ACE2 plasmids were transfected to HeLa cells. HeLa cells were infected 24 h post transfection with Wuhan-hu-1 or WBP-1 at MOI = 1. The cells were fixed 24 h later with 4% paraformaldehyde in PBS for 30 min. ACE2 expression was detected using rabbit anti-ACE2 IgG (Cat No.: A12737, Abclonal, Inc) followed by CoraLite594-conjugated goat anti-rabbit IgG (H+L) (Cat. No: SA00013-4, Proteintech, Wuhan, Hubei, China)). SARS-CoV-2 nucleocapsid expression was detected using mouse anti-NP IgG (Cat. No: 40143-MM08, Sino Biological) followed by CoraLite488-conjugated Affinipure goat anti-mouse IgG (H+L) (Cat. No: SA00013-1, Proteintech). Nuclei were stained with DAPI. All samples were then visualized on Auto Invitrogen EVOS FL Auto Cell Imaging System (Thermo Fisher Scientific).

2.10. Biolayer interferometry (BLI) experiments

The interaction between ACE2 and RBD was analyzed with the Octet Red 96 instrument (Pall ForteBio) using an hFC sensor at 25 °C. Proteins used in the BLI experiment (hACE2, mACE2, WT-RBD, Q493K-RBD, Q498H-RBD, Q493K/Q498H-RBD) were purchased from Sino Biological. Kinetics buffer (phosphate-buffered saline, 0.1% bovine serum albumin, 0.02% Tween) was used in all the experiments. The sensors were dipped in human hACE2-hFC (hACE2) or mouse mACE2-hFC (mACE2) at a concentration of 10 μg/mL. The functionalized sensors were dipped in different RBD concentrations (0, 6.25, 12.5, 25, 50, 100, 200, and 400 nM) during at 180 s interspersed with a rinsing step in the buffer solution. The data traces shown in the graphs were obtained after sensors were exposed to SARS-CoV-2 wild type RBD or mutational RBD proteins, using Data Analysis software v8.1 (ForteBio). The processed data were plotted using Prism 8 (Graphpad Software).

2.11. Validation of R848 against SARS-CoV-2 in vitro

To assess the cytotoxic effect, Caco2 cells were seeded into 96-well plates and treated with R848 (0–80 μM). Following incubation for 48 h, the cytotoxicity was determined using the TransDetect Cell Counting kit (CCK, Transgen, China) according to the manufacturer's instructions. The absorption of the samples was determined at 450 nm with an iMark Macroplate Reader (Bio-Rad, Hercules, CA, USA). To test the antiviral effect of R848 against infection, Caco2 cells were seeded into wells of a 12-well plate and incubated. Cells were treated with R848 (0.2–20 μM) or DMSO for 24 h before infection with viruses at MOI = 1. Infected cells were further incubated in the R848 or DMSO at 37°C. Samples were collected at 48 and 72 hpi, and viral titers were determined through plaque assays.

2.12. R848 antivirus activity in mouse model

Female BALB/c mice (n = 10) aged 4-6 weeks were randomly intranasally infected with 5 LD_{50} of WBP-1 virus in 50 μL DMEM and then they were intraperitoneally injected with R848 (1.5 mg/kg) or PBS immediately [19,20]. Infected mice were further treated with the R848 or PBS once a day for four consecutive days. Mice were monitored for weight loss and survival for 10 days. Three mice in each group were humanely sacrificed on 5 dpi and their lungs were collected for further study. For viral loads determination, each lung was split in half. The right half was collected in 1 mL of PBS containing antibiotics (100 U/mL penicillin-streptomycin). For histopathology analyses, left lungs were fixed in formalin.

2.13. Statistical analysis

In this study, the sample size calculation in mice experiments to find difference between groups was used as mentioned previously [21]. Normal distribution data were conducted using SPSS software. Statistical significance was analyzed using GraphPad Prism version 8.0.2 (San Diego, CA, USA) by applying unpaired Student's t test or one-way analysis of variance (ANOVA) to obtain p values. Two-way ANOVA was used when appropriate. P values lower than 0.05 were considered statistically significant. $*$, $p < 0.05$; $**$, $p < 0.01$; $***$, $p < 0.001$; $****$, $p < 0.0001$. Number of animals in each group and specific details on statistical tests were described in figure legends.

2.14. Role of funders

The funders were not involved in study design, the collection, analysis, or data interpretation; the writing of the report; or the decision to submit the paper for publication.

3. Results

3.1. Generation of a mouse-adapted SARS-CoV-2 strain

To generate a mouse-adapted SARS-CoV-2 strain, the wild type (WT) Wuhan-Hu-1 virus was adapted by serial passage (11 rounds) in mice lungs. Our previous studies have demonstrated that aged BALB/c mice are susceptible to SARS-CoV-2 infection and that the virus replicates better in aged mice than in young ones. Therefore, the first generation of viruses was passaged in 12-month-old BALB/c mice. Lungs were harvested at three days post inoculation (dpi) when peak viral titers were observed, and virions were collected to continue the serial passage via intranasal inoculation in young mice. To screen for virulence and virus replication, three mice were sacrificed at 3 dpi to harvest lungs at passages 2, 5, 8, and 11 (P2, P5, P8, and P11). Each lung was split in half. The right half was used to extract RNA samples for viral RNA load analysis and genome deep sequencing, and the other half was placed in formalin for histopathologic analysis. The three remaining mice from each passage were used to observe for signs of morbidity or mortality. Microscopy showed that P2-infected mice did not exhibit any lung lesions (Fig. 1a). Minor changes characterized by a few thickened alveolar walls with monocyte and lymphocyte infiltration were present in lung tissues of P5-infected mice. Pulmonary lesions in mice became more serious with increasing number of passages. In mice infected with P11 viruses, bronchioles were filled with exfoliated necrotic cells and surrounded by numerous mononuclear lymphocytes. Moreover, thickened alveolar septa and inflammatory cell infiltration were observed, and all mice developed serious interstitial pneumonia. Deaths were not observed in P2, P5, and P8. However, increased morbidity, as indicated by weight loss, slightly bristled fur, lethargy, and decreased response to external stimuli, was noted in P8-inoculated mice at 4 dpi. Extreme morbidity and mortality were observed in P11 mice, among which two out of the three mice died. Viral loads were quantified in lungs through qRT-PCR at 3 dpi (Fig. 1b). Substantial viral RNA was detected after only two passages, and further increased to $10^{9.09}$ copies/g in P5, $10^{9.44}$ copies/g in P8, and $10^{9.50}$ copies/g in P11. The viral RNA load analysis indicated that the mouse-adapted SARS-CoV-2 virus is replication competent and can be stably passaged in lungs. Virus pools derived from serial passages likely acquired mutations that increase their ability to replicate and cause fatal lung infection in mice.

3.2. Identification of mutations in the mouse-adapted virus

We obtained five clonal isolates from the P11 virus pool through three rounds of plaque assays in Vero cells. These five clones were screened for lethality in 4-6 weeks BALB/c mice (n = 3), resulting in 0/3, 1/3, or 2/3 mortality (Fig. 1c). Strain #2, which caused severe morbidity and death within three to five days after intranasal inoculation, was defined as WBP-1 and selected for further analysis. To identify the mutations in WBP-1 responsible for its increased virulence, the genomes of the wild-type Wuhan-Hu-1 and mouse-adapted WBP-1 viruses were sequenced using next-generation sequencing (Fig. 1d). WBP-1 acquired a 740 bp deletion (27326-28065) and ten single nucleotide substitutions, including five synonymous and five nonsynonymous mutations. The deletion spanned multiple accessory genes, including ORF6, ORF7a, ORF7b, and ORF8. The five nonsynonymous mutations were localized to the open reading frame (ORF) 1ab, 3C-like protease ($3CL^{pro}$), non-structural protein 6 (NSP6), non-structural protein 9 (NSP9), and spike (S) protein. Most notably, two of the mutations, C23039A (Q493K) and A23056C (Q498H), were mapped to the RBD of the S protein which is key host determining factor, suggesting that these two mutations is likely responsible for efficient WBP-1 replication in mice.

3.3. Dynamics of mutations in SARS-CoV-2 throughout passage in mice

To understand how mutations arose in SARS-CoV-2 throughout passage in mice during mouse adaptation, we analyzed the genome sequence of SARS-CoV-2 from different passages (Fig. 1e). The whole-genome deep sequencing metrics and quality control were shown in Figure S1 and Table S1, with data from P2 excluded due to its low coverage. P5 viruses showed 21 mutations, including three stable mutations (A8203G, 0.889; T17825C, 0.986; and A23056C, 1.000) and 19 low frequency mutations with rates varying from 0.044118 to 0.272727. To our surprise, in the retrospective analysis, the stable mutation A23056C (Q498H in RBD) dominated after only one passage in aged mice (Figure S2). Another key position in RBD, the C23039A (Q493K) mutation which probably mediates the virus binding affinity with mACE2, began to appear in the P5 viral gene pool. Going from P5 to P8, only nine out of the 21 P5 mutations persisted while another eight new mutations appeared. P11 harbored a total of thirteen mutations, all of which could be traced back to P8. In particular, three of the thirteen P11 variations (C1912T, C12915T, C23039A) increased frequency going from P8 to P11; two of those three changes C12915T (T77I in NSP9) and C23039A (Q493K in RBD) are nonsynonymous and likely contribute to the high pathogenicity of WBP-1 in mice. Novel mutations in P5, P8 and P11 (i.e. 21 vs 8 vs 0) decreased rapidly in numbers, suggesting that the viral genome become stabilized towards the end of adaptation, with selection pressures mainly due to host-related differences. Therefore, our dynamic mutation analysis allowed us to dissect the intricate evolutionary processes of SARS-CoV-2 in an unnatural host.

3.4. Mouse-adapted SARS-CoV-2 pathogenesis in BALB/c mice

To investigate the pathological characteristics of BALB/c mice infected with the mouse-adapted SARS-CoV-2, groups of mice (n = 5)

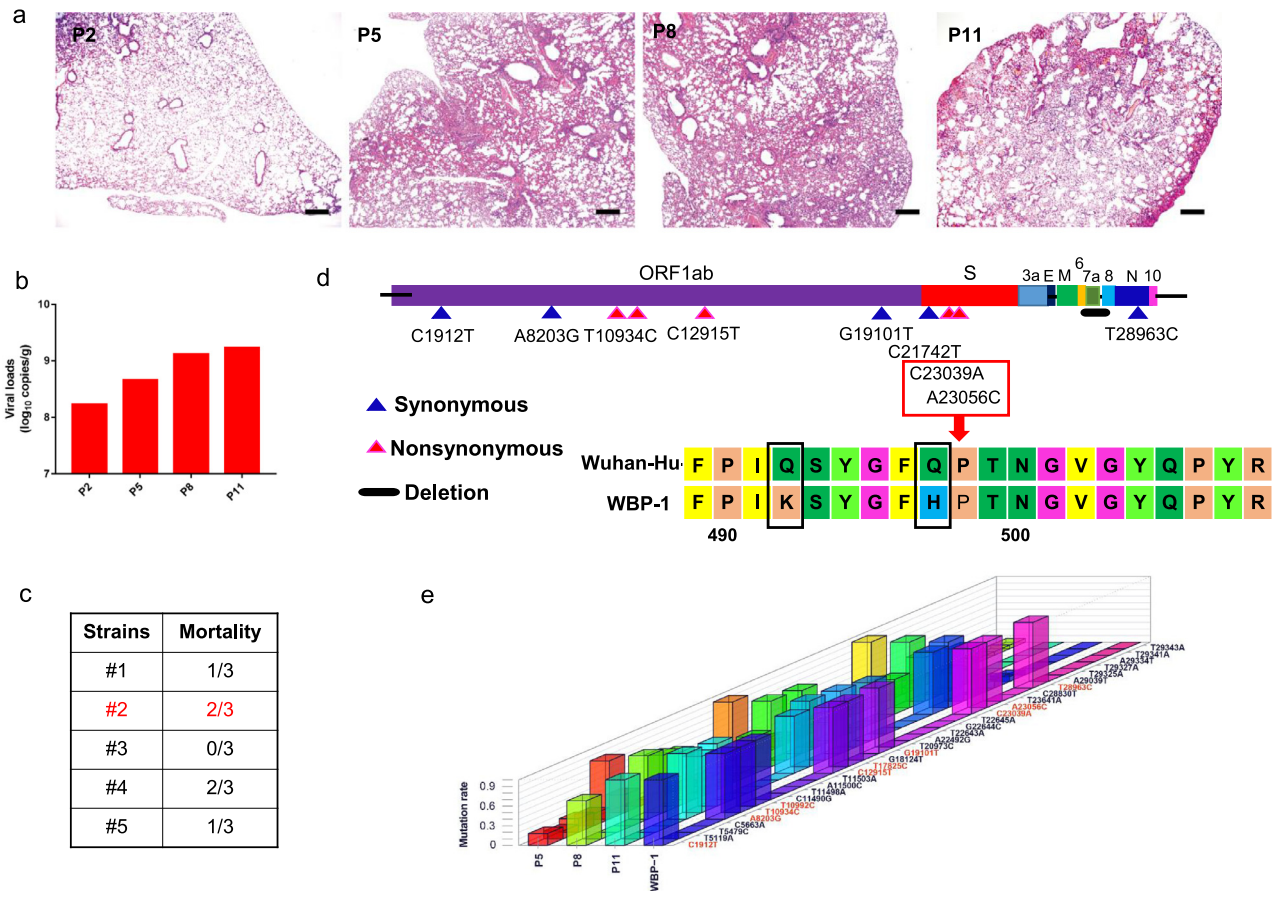

Strains	Mortality
#1	1/3
#2	2/3
#3	0/3
#4	2/3
#5	1/3

Fig. 1. Generation of mouse-adapted SARS-CoV-2 WBP-1. Wild type (WT) Wuhan-Hu-1 was passaged in old and young mice to obtain WBP-1 that was adapted to cause respiratory disease in mice. (a) Hematoxylin and eosin (H&E) staining of lung sections from mice infected with virus obtained through different passages (P2, P5, P8, P11) of SARS-CoV-2. Scale bars, 100 μm. (b) Viral copies were detected through qRT-PCR at three days post infection (dpi) in the lungs. (c) Five clonal isolates were obtained from the P11 virus pool by three rounds of plaque purification in Vero cells. The strain #2 that showed a high mortality rate in mice was defined as WBP-1. (d) Location of the mutations and deletion in the genome of WBP-1. WBP-1 obtained five synonymous (purple triangles), five nonsynonymous (red triangles), and a 740 bp deletion (black line). (e) Mutational frequency during SARS-CoV-2 experimental passage in pooled mouse groups. Single nucleotide variants are represented along the genome for the mice of passage 5, passage 8, passage 11 and WBP-1 virus.

were intranasally infected with 10-fold serial dilutions of the WBP-1 virus (i.e. 10^5 to 10^2 PFU). The infected mice were observed for weight loss and survival for 10 dpi. Mice experiencing weight loss in excess of 20% of the initial body weight were euthanized according to our animal study protocol. All groups of infected mice began to lose weight at 2 dpi (Fig. 2a). Mice infected with a lethal dose (10^5 PFU) lost more than 20% of the initial body weight at 4 dpi. Mice infected with a non-lethal dose (10^3 PFU) lost approximately 4.2% of the initial body weight at 4 dpi. At the lowest dose (10^2 PFU), the weight loss was not significant. The surviving mice began to regain weight after 5 dpi and returned to their preinfection weight at 7 dpi. Notably, the group of mice receiving a dose of 10^5 PFU WBP-1 virus all died (5/5) by 5 dpi (Fig. 2b). Two out of five mice survived in the group administered 10^4 PFU virus. The LD_{50} of WBP-1 was calculated to be $10^{3.8}$ PFU.

To further examine if SARS-CoV-2 infection caused the pathological features of pneumonia in mice similar to those in human, mice (n = 6) were intranasally infected with 50 μL of 2 LD_{50} of WBP-1. Mice in the control group were mock-infected with DMEM. Clinical signs of infection were observed in infected mice at 2 dpi. Mice were sacrificed at 3 and 5 dpi to harvest various organs for pathogenicity analysis and determination of viral loads. High viral loads were observed in the trachea and lung of WBP-1 infected mice, while trace amounts of viral nucleic acid was detectable in turbinate, heart, and spleen. In particular, lung tissues had the highest viral RNA copies ($10^{9.5}$ copies/g), which remained very little changed from 3 dpi to 5 dpi (Fig. 2c). Infectious virion titer calculated through plaque assays were similar to viral RNA copies (Fig. 2d).

Next, we determined the mRNA expression of cytokines induced by SAR2-CoV-2 in the lung (Fig. 2e). The expression levels of IL1β ($P < 0.0001$), TNFα ($P = 0.0018$), MCP1 ($P = 0.0399$), and IL10 ($P < 0.0001$) in WBP-1-infected mice were significantly elevated compared to those in mock-treated mice. To further determine whether these mice had pneumonia, lung tissues collected at 3 and 5 dpi were subjected to analysis via histopathological H&E staining. Acute stage lung damage was noted as firm, red, heavy lobes in the pathological autopsy of mice. Microscopy showed moderate interstitial pneumonia with thickened alveolar septa at 3 dpi. Inflammatory cell infiltration was also identified in the lung tissues of infected mice, but not in those of control mice. The histopathologic analysis of lung tissues from 5dpi showed severe pneumonia (Fig. 2f). The bronchioles were filled with exfoliated necrotic cells (black arrow) and surrounded by numerous mononuclear lymphocytes (green arrow). Moreover, there were abundant lymphocytes around small blood vessels. The alveoli were filled with a large amount of inflammatory exudate (red arrow). Interestingly, this mouse model successfully reproduced inflammatory pulmonary vascular thrombosis (blue arrow) that were reported in human and rhesus macaques [22,23]. Alveolar septa thickened, and more importantly, necrotic cells and debris built up creating pus and filling the small airways as pneumonia continued to develop. These multiple factors led to lung consolidation associated with defects in lung function. No obvious pathological changes were observed in other organs (heart, liver, spleen, kidney, brain, intestine and uterus) (Figure S3). When immunohistochemistry was used to confirm viral replication, cells in the

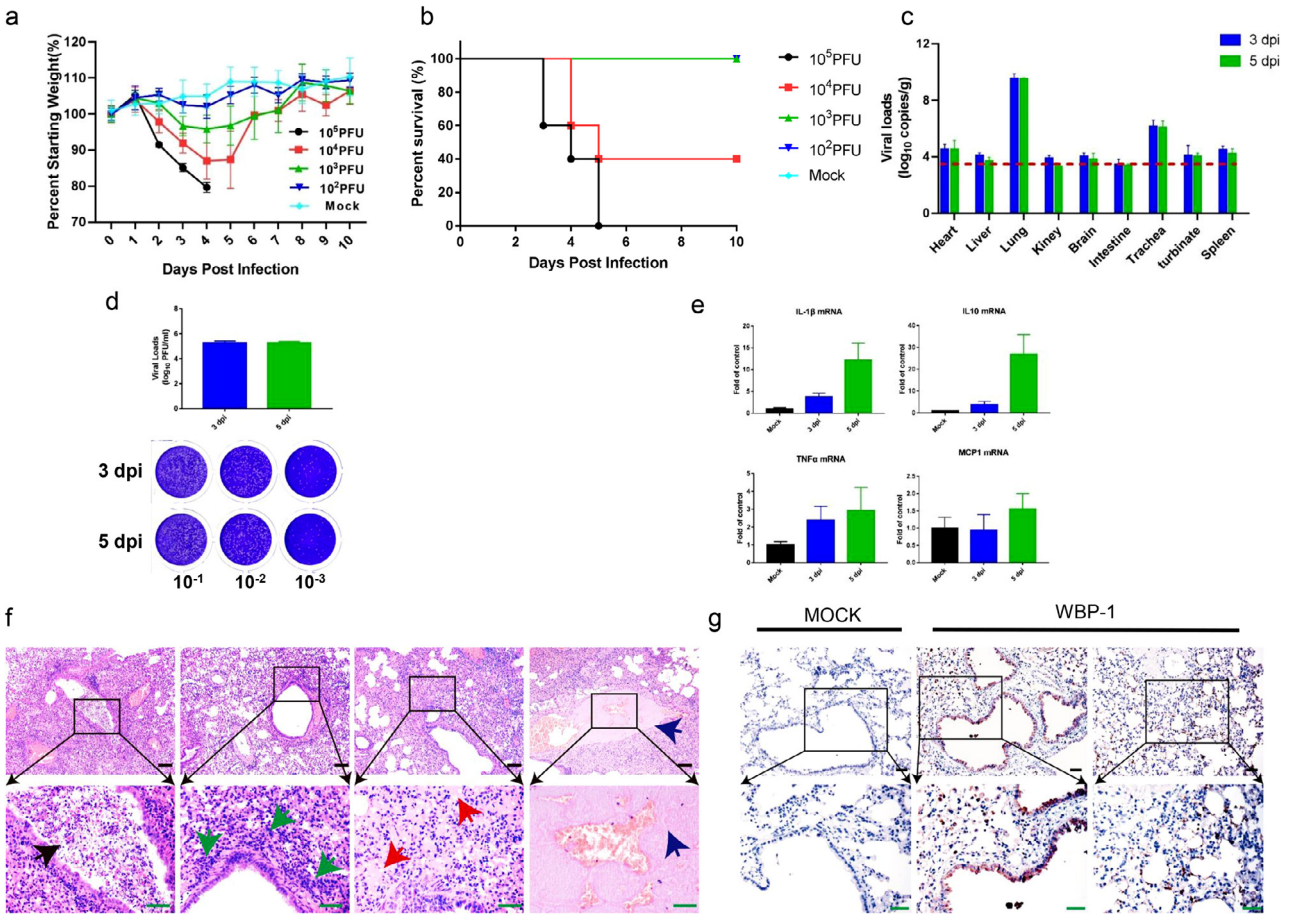

Fig. 2. Characterization of mouse-adapted SARS-CoV-2 WBP-1 in mice. (a, b) Groups of mice (n = 5) were intranasally infected with 10-fold serial dilutions of WBP-1 virus. The infected mice were observed for weight loss and survival for 10 dpi. (c- f) Mice (n = 6) were intranasally infected with 2 LD_{50} of the WBP-1 virus and mice in the control group were mock-infected with DMEM. (c) Viral RNA copies were determined through qRT-PCR at 3 and 5 dpi in the heart, liver, lung, kidney, brain, intestine, trachea, turbinate, and spleen of WBP-1. (d) Viral titers in the lung were determined through plaque assays. (e) Cytokine (IL1β, TNFα, MCP1, and IL10) mRNA levels in the lung were evaluated at 3 and 5 dpi. Statistical significance was analyzed by unpaired Student's t tests. $^{*}p < 0.05$; $^{**}p < 0.01$; $^{***}p < 0.001$ $^{****}p < 0.0001$. (f) Hematoxylin and eosin (H&E) staining of lung sections from mice infected Mouse-adapted WBP-1 virus (Exfoliated necrotic cells, black arrow; Mononuclear lymphocytes, green arrow; Inflammatory exudate, red arrow; Vascular thrombosis, blue arrow). Scale bars (black), 100 μm. Scale bars (green), 50 μm. (g) Immunohistochemical detection of viral antigen using anti-Spike protein Rabbit monoclonal antibody in bronchi and alveoli. Scale bars (black), 100 μm. Scale bars (green), 50 μm.

bronchiolar ciliated and alveolar epithelial were positive for SARS-CoV-2 S antigen (Fig. 2g) in infected mice, but not in the mock-infected control. In the lesional areas of the lungs, sequential IHC-stained sections revealed viral antigens in macrophages, alveolar epithelia, and degenerative and desquamating bronchial epithelial cells. Viral antigens were undetectable in the heart, liver, spleen, kidney, brain, and intestine (data not shown). Consequently, WBP-1 in mice reproduced pathogenic characteristics that closely resemble the many human COVID-19 clinical manifestations, including morbidity, mortality, and pulmonary pathology.

3.5. Mouse adapted WBP-1 virus used mouse ACE2 to gain access to cells

To investigate whether the mouse-adapted WBP-1 viral strain, which acquired Q493K and Q498H mutations in RBD, use mouse ACE2 (mACE2) to enter the cell, Hela cells were infected with Wuhan-Hu-1 or WBP-1 viruses after transfection of hACE2 or mACE2 expressing plasmids (Fig. 3). Wuhan-Hu-1 or WBP-1 virus NP was not detected in control plates transfected with p3XFLAG. In the hACE2 group, both Wuhan-Hu-1 and WBP-1 viruses could enter and replicate in Hela cells. In mACE2 expressing cells, however, only mouse adapted virus WBP-1 but not parent strain Wuhan-Hu-1 could infect. Collectively, these results clearly demonstrate that WBP-1 is capable of using mouse ACE2 to gain access to host cells, while its ability to infect human cells are not altered.

3.6. Mouse adapted WBP-1 RBD binds to mouse ACE2

To determine the impact of two acquired amino acid mutations in the WBP-1 RBD on the ability of the mouse-adapted virus to utilize mACE2 as a receptor, structural modeling was performed using the RBD: hACE2 structure as a reference (Fig. 4a). Structure remodeling suggested the binding affinity of Q493K/Q498H-RBD to hACE2 were almost unchanged compared to that of WT RBD (Fig. 4b). However, molecular modelling of the receptor interface predicted no interaction between Wuhan-Hu-1 RBD and with mouse ACE2 (Fig. 4c). The substitution of residue Q493K interact with N71 of mouse ACE2 via H-bond. Q498H interacting with Y41 was found to form a solid pi-bond interaction (Fig. 4d).

Next, we determined the binding affinity of WBP-1 RBD to mACE2 using biolayer interferometry (BLI) (Fig. 4e-l). The human Fc (hFc)-tagged ACE2s were first captured by sensors preimmobilized with anti-human IgG antibodies, and then the serially diluted RBDs were added to the plates. Consistent with our hypothesis, mACE2 interacted with Q493K-RBD (Fig. 4e), Q498H-RBD (Fig. 4f), Q493K/Q498H-RBD (Fig. 4g) with an equilibrium dissociation constant (K_D) of 2.68×10^{-9}, 1.23×10^{-9} and 1.04×10^{-9}, respectively, with the

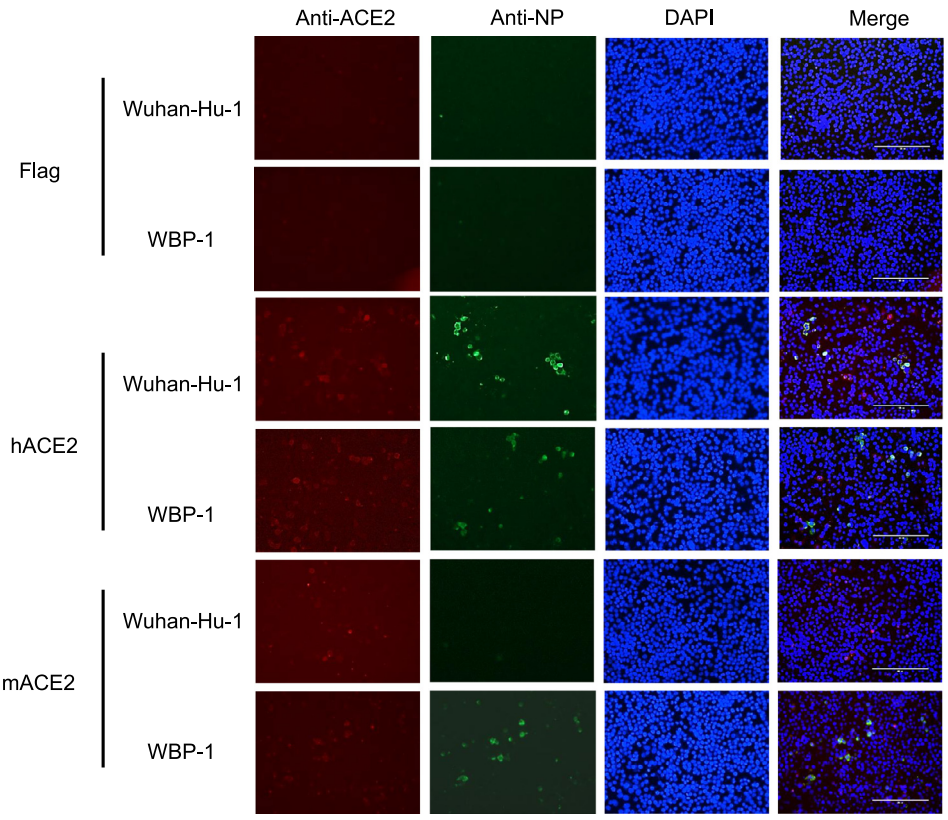

Fig. 3. WBP-1 virus using mouse ACE2 to gain access to cells was determined by immunofluorescence. Hela cells with transfection of empty vector (Flag), hACE2, or mACE2 plasmids were infected with WT Wuhan-Hu-1 or mouse-adapted WBP-1. ACE2 expression was detcted using rabbit anti-ACE2 IgG followed by CoraLite594-conjugated goat anti-rabbit IgG (H+L). SARS-CoV-2 nucleocapsid expression was detected using mouse anti-NP IgG followed by CoraLite488-conjugated Affinipure goat anti-mouse IgG(H+L). Nuclei were stained with DAPI. Scale bars, 200 μm.

double mutant Q493K/Q498H-RBD being the strongest binder. No binding between the mACE2 and the WT-RBD (Fig. 4h) was detected through BLI experiments. Next, BLI was performed to determine if the two mutations affect RBD binding to human ACE2 (Fig. 4i-l). The result showed that neither Q493K nor Q498H had a substantial effect on the RBD binding affinity with hACE2. Although Q493K and Q498H were able to increase RBD binding affinities with mACE2, they were substantially lower than that with hACE2.

3.7. *R848 inhibits SARS-CoV-2* in vitro *and* in vivo

TLR7/8 agonist R848 has been explored as an antiviral therapeutic agent against HIV-1, Zika, HBV, and MNV viruses. We found that at concentrations without obvious cytotoxicity (Figure S4a), R848 exhibited dose-response inhibition of SARS-CoV-2 (Wuhan-Hu-1) replication in vitro (Fig. 5a, S4b). Then we tested whether R848 could also inhibit the replication of mouse-adapted WBP-1 SARS-CoV-2 in the mouse model. Mice were intraperitoneally injected with R848 after immediately intranasal infection with the WBP-1 virus, and further treated with R848 or PBS once a day for four consecutive days. The two groups of mice infected with WBP-1, regardless of treatment with PBS or R848, showed drastic weight loss at day 2 dpi (Fig. 5b). However, R848-treated mice began to gain weight after 3 dpi and showed better mental state than those in the PBS group (Figs. S5). R848-treated mice in PBS group showed bristled fur, severe body weight loss, breathing difficulties, depressed spirits and lethality. Almost no clinical symptoms appeared in R848-treated mice. All mice in the R848 group survived and regained their original weight at 6 dpi, but all mice in the PBS group were dead by 6 dpi (Fig. 5c). Three mice in the each group were sacrificed 5 dpi, and their lungs and tracheas were collected for viral load determination and histopathology analysis (Figs. 5d). The level of lung viral loads in the R848 group ($10^{5.0}$ copies/g) remained significantly ($P < 0.0001$) lower than those observed in mice of the PBS group ($10^{9.2}$ copies/g). Interestingly, R848 inhibited the replication of mouse-adapted SARS-CoV-2 in the trachea ($P < 0.0211$), but failed to do so in the nasal turbinate ($P = 0.6169$). Histopathology analysis showed that inflammatory lung injury and thickened alveolar septa was less severe in R848-treated mice than that in the PBS group (Fig. 5e). Therefore, these results demonstrated that the WBP-1 virus mouse model could serve as a platform for assessing SARS-CoV-2 therapeutics.

4. Discussion

Mouse-adapted viruses were available for both MERS-CoV and SARS-CoV [24,25]. Both MERS-15 (MERS-CoV) and MA15 (SARS-CoV) viruses were obtained after 15 passages in young adult mice. Recently, several mouse-adapted SARS-CoV-2 strains were produced through either reverse genetics or passaging in mice [4,15,26,27]. Through the latter approach, MASCp6, MA10, and HRB26 were generated after 6, 10, and 15 passages, respectively. Herein, we produced WBP-1 after 11 passages in mice. The fewer number of passages used for SARS-CoV-2 adaption suggests that compared to MERS-CoV and SARS-CoV, SARS-CoV-2 is more likely to mutate to produce viruses that are capable of infecting mice. Elder human populations are most susceptible to SARS-CoV-2 and develop a more serious disease with higher mortality [28]. Likewise, our previous studies demonstrated that aged mice were susceptible to SARS-CoV-2 and the virus replicated better in aged mice than in young ones (unpublished results). In this study, the lungs in aged mice infected with Wuhan-Hu-1 (i.e. P1 passage) had peak viral titers ($10^{4.77\sim5.05}$ PFU/mL) at 3 dpi, and then decreased loads ($10^{1.85\sim2.17}$ PFU/mL) at 5 dpi. In contrast to old

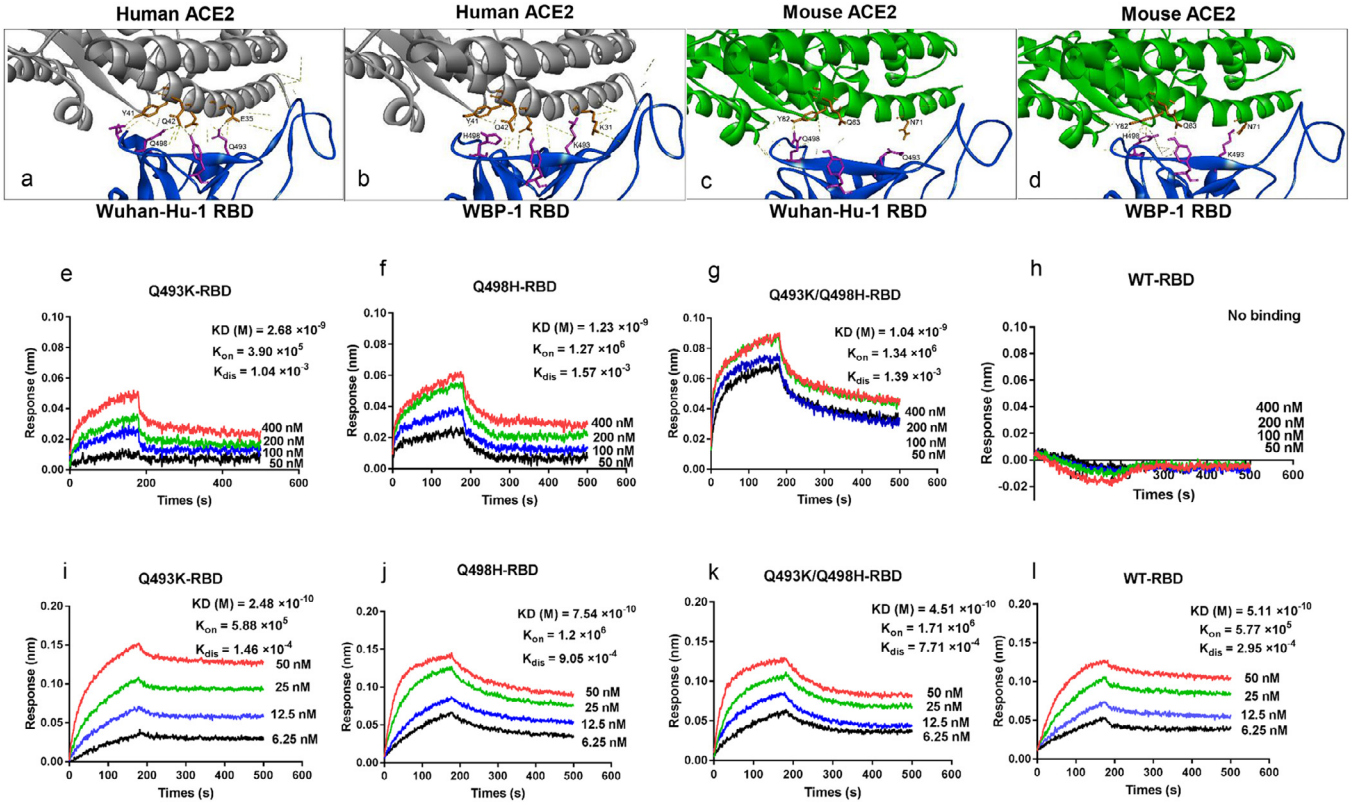

Fig. 4. Mouse-adapted WBP-1 virus RBD enhance interactive affinities with mACE2. (a-d) Modelling of SARS-CoV-2 RBD−ACE2 interface. (a) Wuhan-Hu-1 RBD interacts with of human ACE2. (b) WBP-1 RBD (Q493K/Q498H-RBD) interacts human ACE2. (c) Modelling of Wuhan-Hu-1 RBD and mouse ACE2. (d) Modelling of WBP-1 RBD (Q493K/Q498H-RBD) shows interaction with mouse ACE2. (e-l) The binding affinities of the RBD of WBP-1 and mACE2 or hACE2 were determined through BLI experiments. The sensors were dipped in mACE2-hFC and functionalized sensorgrams captured upon incubation of Q493K-RBD (e), Q498H-RBD (f), Q493K/Q498H-RBD (g), and WT-RBD (h) at 6.25 (black), 12.5 (blue), 25 (green), and 50 nM (red). The sensors were dipped in hACE2-hFC and functionalized sensorgrams captured upon incubation of Q493K-RBD (i), Q498H-RBD (j), Q493K/Q498H-RBD (k), and WT-RBD (l) at 50 (black), 100 (blue), 200 (green), and 400 nM (red).

mice, young mice infected with Wuhan-Hu-1 had much lower viral titers ($10^{1.95–2.60}$ PFU/mL) at 3 dpi and no detectable titers at 5 dpi. Therefore, the first generation of viruses passaged in 12-month-old BALB /c mice were harvested at 3 dpi to obtain more virions for continued serial passage in young mice.

Mouse-adapted WBP-1 virus acquired a deletion and five amino acid substitutions in $3CL^{pro}$, NSP6, NSP9, and S proteins. The NSP6 protein of SARS-CoV-2 is a multi-pass transmembrane protein and it has been shown to antagonize IFN-I production by binding TANK-binding kinase 1 to suppress interferon regulatory factor 3 phosphorylation [29–31]. NSP6 is targeted to the endoplasmic reticulum where it induces the formation of autophagosomes [32]. Therefore, mutations in NSP6 may affect viral autophagy. It has also been shown that NSP6, together with NSP3 and NSP4, induce double-membrane vesicles that anchor the RNA replication complex during SARS-CoV coronavirus infection [33]. However, the I7T mutation is located in vesicular lumen, and therefore this mutation probably has little effect on its viral RNA replication. The $3CL^{pro}$ is essential for viral polyprotein maturation during viral replication and considered as a promising drug target. The mutation F294L, which is located in helix 11, is ~30-Å away from the catalytic active site and therefore should not affect proteolytic activity of $3CL^{pro}$ [34]. A previous study investigated mutational frequencies of 579 complete SARS-CoV-2 genome sequences and indicated that NSP9 is highly conserved [35]. The function of NSP9 remains unclear, but is related to viral RNA synthesis [36]. Moreover, NSP9 binds RNA and interacts with NSP8 (RNA dependent RNA polymerase cofactor), which may be essential for its function [37]. NSP9 is associated with the virulence of mouse-adapted SARS-CoV in young mice [38]. In this study, the contributions of T77I in NSP9 to SARS-CoV-2 mouse adaptation or viral pathogenesis should be further investigated. In addition, WBP-1 virus bearing a 740bp deletion truncates open ORF6 and removes the ORF7a, ORF7b, and ORF8. Interestingly, as shown in Figure S1a, P2 viruses acquired the deletion with mutation rates at 100%. SARS-CoV-2 ORF6 was demonstrated the strong suppression on interferon signaling [39]. It is not clear whether the remaining ORF6 truncation in WBP-1 virus will maintain the similar function. SARS-CoV-2 variants with ORF7b/8 deletions of various lengths have been detected in different regions [40]. Complete or partial ORF8 deletions were also observed in SARS-CoV [41–43]. Frequent deletions around the ORF8 gene suggested that it was an evolutionary hot spot for adaptation of SARS-CoV to hosts [42]. SARS-CoV-2 variants with a 382-nucleotide deletion in the ORF8 result in a milder clinical illness than that caused by the wild-type virus [44].

Several mouse-adapted SARS-CoV-2 strains, such as MASCp6 (N501Y), MA10 (Q493K) and HRB26 (Q498H), increase virulence or replication in mice likely attributed to one of the mutations in the S protein [15,26,45,46]. The mutations N501Y, Q493K, or Q498H were predicted to enhance interactions with the mACE2 receptor. Interestingly, WBP-1 acquired both Q493K and Q498H mutations simultaneously. In this study, we experimentally determined the binding affinities and demonstrated for the first time that Q493K, Q498H, or both increased the interactive affinities of RBD with mACE2. Although these mouse-adapted SARS-CoV-2 strains all replicate efficiently in the lung of mice, MASCp6 and HRB26 only cause mild pathological changes in lung and produce no obvious clinical symptoms of respiratory disease [15,26]. For reported mouse-adapted strains. High-titer virus replication was observed in lung tissue at 2 or 3 dpi and decreased by 4 or 5 dpi. In comparison, High viral loads were observed in the lung of WBP-1 infected mice and remained little

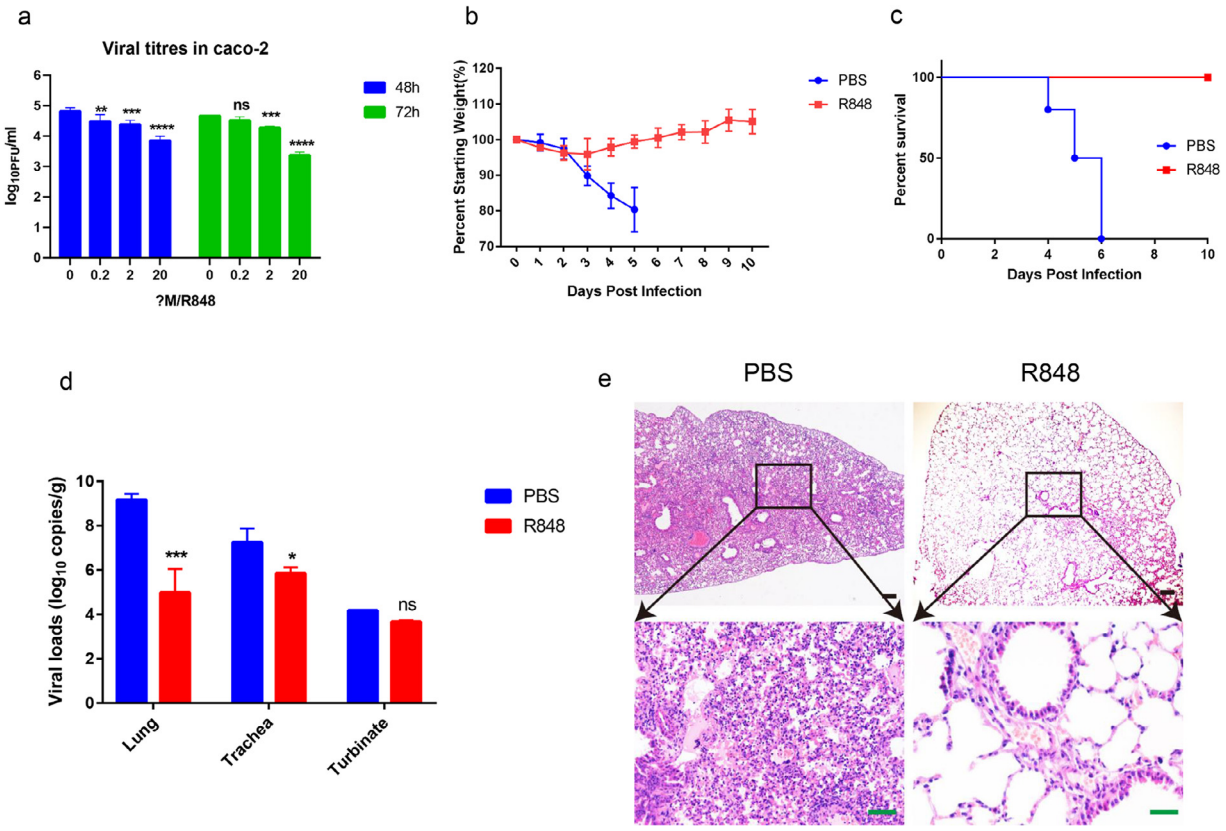

Fig. 5. R848 inhibits SARS-CoV-2 *in vitro* and *in vivo*. (a) Caco2 cells were treated with R848 (0-20 μM) for 24 h before infection with viruses at a multiplicity of infection (MOI) of 1. Infected cells were further incubated in the R848. Samples were collected at 48 and 72 h post infection (hpi) and viral titers were determined using plaque assays. (b-e) (n = 10) Mice were intraperitoneally injected with R848 after immediately intranasal infection with the WBP-1 virus. Infected mice were further treated with the R848 or PBS once a day for four consecutive days. Mice were monitored for weight loss (b) and survival (c) for 10 days. (d) Viral loads in mice lung, trachea and turbinate were determined at 5 dpi. (e) Hematoxylin and eosin (H&E) staining of lung sections from PBS or R848 treated mice. Scale bars (black), 100 μm. Scale bars (green), 50 μm. (a) and (d), Log transformed data analyzed by Two-way ANOVA followed by Sidak's multiple comparisons. The line represents the mean and error bars represent standard deviation. $^{*}p < 0.05$; $^{**}p < 0.01$; $^{***}p < 0.001$ $^{****}p < 0.0001$.

changed from 3 dpi to 5 dpi. Moreover, WBP-1 causes more serious pathogenic indices (bristled fur, depressed spirits, body weight loss, high reproduction in lung, lung damage, and lethality) in mice. Interestingly, this mouse model also successfully reproduced inflammatory pulmonary vascular thrombosis that was reported in human and rhesus macaques. Syrian hamster model for SARSCoV-2 infection failed to replicate the symptoms of severe case and even death, though it recapitulated the clinical, virological, histopathological, and immunological characteristics of human disease [47]. We assessed the LD_{50} of the WBP-1 was determined to be $10^{3.8}$ PFU, and mice infected with 2 LD_{50} showed large pneumocyte degeneration and necrosis in the lung. In addition, WBP-1 virus growth in Vero cells is similar to that of Wuhan-Hu-1 virus. According to 2019 Novel Coronavirus Resource of China National Center for Bioinformation, a total of 1605 amino acid changes are identified in S protein, of which, 204 located in the RBD (https://bigd.big.ac.cn/ncov/protein). It is worth noting that eight SARS-CoV-2 strains from several countries have naturally acquired Q493K mutation in RBD which may allow the virus to bind mACE2 and infect mice. Therefore, we propose that the Q493K and Q498H mutations in RBD could serve as an indicator for recognizing SARS-CoV-2 variants with potential public health risk that could emerge at the human-mouse interface.

Using WBP-1 and BALB/c mice, we demonstrated that the antiviral compound R848 (Resiquimod) can be used to effectively treat SARS-CoV-2 infection. As a dual TLR7/TLR8 agonist, R848 is used as a drug to help treat topical viral infections, tumors and asthma, or as an adjuvant to increase the effective of vaccines [48]. The activation of Toll-like receptors triggers a signaling cascade that leads to the production of interferon-stimulated genes and proinflammatory cytokines with antiviral activities. R848 have been reported to inhibit the herpes simplex virus-type-1 and -2, HIV-1, Zika, and hepatitis B viruses in *vitro* [48–51], but, there are few reports regarding the antiviral activity of R848 *in vivo*. Zhao et al. found that the intranasal pretreatment of aged mice with R848 provided a certain level of protection against lethal SARS-CoV or influenza A virus challenges [51]. Herein, we verified the antiviral activity of R848 against SARS-CoV-2 *in vitro* and *in vivo*. It is worth noting that our initial test using Vero cells was not successful, possibly due to a failure to produce interferon-stimulated genes that interferes with specific steps of viral replication in the IFN-deficient Vero cell line. Moreover, R848 inhibited the replication of mouse-adapted SARS-CoV-2 in the lung and trachea, but failed to do so in the nasal turbinate. Similarly, postchallenge neutralizing antibodies therapy reduces SARS-CoV-2 infection in the lungs but considerably less in nasal turbinate [21]. Tian et al. suggested that immunosuppression occurs in the early stage of COVID-19 infection and then an activated immune response emerges in severely affected patients [52]. The cytokine storm symptoms in COVID-19 have promoted the use of potent immunomodulatory therapies in clinical trials and on a compassionate basis [53]. Considering that R848 is an immunomodulator that activates host immune responses, it may be suitable for prophylaxis or early treatment before patients develop severe clinical symptoms. Our results suggest that intraperitoneally delivered R848 should be further investigated for lack of clinical data on the use of R848.

In summary, we generated a mouse-adapted WBP-1 virus that produces severe lung infections in mice that closely recapitulate lung pathologies and symptoms caused by COVID-19 in humans. The availability of a small animal model for SARS-CoV-2 with a severe disease phenotype provides a valuable tool for the evaluation of novel antiviral and vaccine strategies, especially in determining the immunopathological consequences of any intervention. We characterized the dynamics of the adaptive mutations in SARS-CoV-2 and demonstrated for the first time that the Q493K and Q498H mutations in the RBD of WBP-1 enhanced its interactive affinities with mACE2. This study also verified the antiviral activity of Resiquimod against SARS-CoV-2 using this mouse model. Additionally, further studies of the viral mutations associated with mouse adaptation may provide new insights into virulence determinants as well as virus host interaction.

Data sharing

The datasets generated in this study are available from the corresponding author on reasonable request.

Contributors

Conceptualization, K.H., Y.Z., Z.Z. and M.J.; Virus infection experiments in vitro and in vivo, K.H., X.H., Y.Z. Y.Z. and X.C.; Viral RNA copies determination, Z.Z., W.G., K.H., X.S.; Histopathology and immunohistochemistry, Y.Z., T.W., Y.Y. and K.H.; Indirect immunofluorescence analysis, K.H., X.H. and Y.Y.; Biolayer interferometry experiments, S.Z., K.H., and Y.Z.; Manuscript writing, K.H., Z.Z., Y.Z., Y. J.T. and M.J.; Resources: M.J., H.C. and F.D. All authors provided revisions and comments. All authors read and approved the final version of the manuscript.

Declaration of Competing Interest

The authors declare no competing interests.

Acknowledgments

This research was funded by the National Key Research and Development Program of China (2020YFC0845600) and Emergency Science and Technology Project of Hubei Province (2020FCA046) and Robert A. Welch Foundation (C-1565). We thank all the members of the M.J. laboratory for helpful feedback. We thank biosafety level 3 (BSL3) facility and State Key Laboratory of Agricultural Microbiology in Huazhong Agricultural University. We thank State Key Laboratory of Virology and National Virus Resource Center in Wuhan Institute of Virology, Chinese Academy of Sciences for providing Wuhan-Hu-1 virus. We also thank professor Guiqing Peng offering lots of advice and help.

Supplementary materials

Supplementary material associated with this article can be found in the online version at doi:10.1016/j.ebiom.2021.103381.

References

[1] Zhu N, Zhang D, Wang W, Li X, Yang B, Song J, et al. A novel coronavirus from patients with pneumonia in China, 2019. N Engl J Med 2020;382(8):727–33.
[2] Guan WJ, Ni ZY, Hu Y, Liang WH, Ou CQ, He JX, et al. Clinical characteristics of coronavirus disease 2019 in China. N Engl J Med 2020;382(18):1708–20.
[3] Kim YI, Kim SG, Kim SM, Kim EH, Park SJ, Yu KM, et al. Infection and rapid transmission of SARS-CoV-2 in Ferrets. Cell Host Microbe 2020;27(5) 704-9 e2.
[4] Sun SH, Chen Q, Gu HJ, Yang G, Wang YX, Huang XY, et al. A mouse model of SARS-CoV-2 infection and pathogenesis. Cell Host Microbe 2020;28(1) 124-33 e4.
[5] Shan C, Yao YF, Yang XL, Zhou YW, Gao G, Peng Y, et al. Infection with novel coronavirus (SARS-CoV-2) causes pneumonia in Rhesus macaques. Cell Res 2020;30(8):670–7.
[6] Sia SF, Yan LM, Chin AWH, Fung K, Choy KT, Wong AYL, et al. Pathogenesis and transmission of SARS-CoV-2 in golden hamsters. Nature 2020;583(7818):834–8.
[7] Imai M, Iwatsuki-Horimoto K, Hatta M, Loeber S, Halfmann PJ, Nakajima N, et al. Syrian hamsters as a small animal model for SARS-CoV-2 infection and countermeasure development. Proc Natl Acad Sci U S A. 2020;117(28):16587–95.
[8] Chandrashekar A, Liu J, Martinot AJ, McMahan K, Mercado NB, Peter L, et al. SARS-CoV-2 infection protects against rechallenge in rhesus macaques. Science 2020;369(6505):812–7.
[9] Rockx B, Kuiken T, Herfst S, Bestebroer T, Lamers MM, Oude Munnink BB, et al. Comparative pathogenesis of COVID-19, MERS, and SARS in a nonhuman primate model. Science 2020;368(6494):1012–5.
[10] Zhou P, Yang XL, Wang XG, Hu B, Zhang L, Zhang W, et al. A pneumonia outbreak associated with a new coronavirus of probable bat origin. Nature 2020;579(7798):270–3.
[11] Bao L, Deng W, Huang B, Gao H, Liu J, Ren L, et al. The pathogenicity of SARS-CoV-2 in hACE2 transgenic mice. Nature 2020;583(7818):830–3.
[12] Sun J, Zhuang Z, Zheng J, Li K, Wong RL, Liu D, et al. Generation of a broadly useful model for COVID-19 pathogenesis, vaccination, and treatment. Cell 2020;182(3) 734-43 e5.
[13] Dinnon KH, Leist SR, Schafer A, Edwards CE, Martinez DR, Montgomery SA, et al. A mouse-adapted SARS-CoV-2 model for the evaluation of COVID-19 medical countermeasures. bioRxiv 2020.
[14] 3rd Dinnon KH, Leist SR, Schafer A, Edwards CE, Martinez DR, Montgomery SA, et al. A mouse-adapted model of SARS-CoV-2 to test COVID-19 countermeasures. Nature 2020;586(7830):560–6.
[15] Wang J, Shuai L, Wang C, Liu R, He X, Zhang X, et al. Mouse-adapted SARS-CoV-2 replicates efficiently in the upper and lower respiratory tract of BALB/c and C57BL/6J mice. Protein Cell 2020;11(10):776–82.
[16] Langmead B, Salzberg SL. Fast gapped-read alignment with Bowtie 2. Nat Methods 2012;9(4):357–9.
[17] Wilm A, Aw PP, Bertrand D, Yeo GH, Ong SH, Wong CH, et al. LoFreq: a sequence-quality aware, ultra-sensitive variant caller for uncovering cell-population heterogeneity from high-throughput sequencing datasets. Nucleic Acids Res 2012;40(22):11189–201.
[18] Cheever FS. General principles of the laboratory diagnosis of viral infections. N Engl J Med 1947;237(16):584–90.
[19] Karadimou G, Gisterà A, Gallina A, Caravaca A, Centa M, Salagianni M, et al. Treatment with a Toll-like Receptor 7 ligand evokes protective immunity against atherosclerosis in hypercholesterolaemic mice. J Internal Med 2020;288(3):321–34.
[20] Zhao J, Wohlford-Lenane C, Zhao J, Fleming E, Lane T, McCray P, et al. Intranasal treatment with poly(I•C) protects aged mice from lethal respiratory virus infections. J Virol 2012;86(21):11416–24.
[21] Zhou D, Chan J, Zhou B, Zhou R, Li S, Shan S, et al. Robust SARS-CoV-2 infection in nasal turbinates after treatment with systemic neutralizing antibodies. Cell Host Microbe 2021.
[22] Ackermann M, Verleden S, Kuehnel M, Haverich A, Welte T, Laenger F, et al. Pulmonary vascular endothelialitis, thrombosis, and angiogenesis in COVID-19. New Eng J Med 2020;383(2):120–8.
[23] Aid M, Busman-Sahay K, Vidal S, Maliga Z, Bondoc S, Starke C, et al. Vascular disease and thrombosis in SARS-CoV-2-infected rhesus macaques. Cell 2020;183(5):1354–66 e13.
[24] Roberts A, Deming D, Paddock C, Cheng A, Yount B, Vogel L, et al. A mouse-adapted SARS-coronavirus causes disease and mortality in BALB/c mice. PLoS Pathogens 2007;3(1):e5.
[25] Cockrell A, Yount B, Scobey T, Jensen K, Douglas M, Beall A, et al. A mouse model for MERS coronavirus-induced acute respiratory distress syndrome. Nat Microbiol 2016;2:16226.
[26] Gu H, Chen Q, Yang G, He L, Fan H, Deng Y, et al. Adaptation of SARS-CoV-2 in BALB/c mice for testing vaccine efficacy. Science 2020;369(6511):1603–7 (New York, NY).
[27] Leist S, Dinnon K, Schäfer A, Tse L, Okuda K, Hou Y, et al. A Mouse-adapted SARS-CoV-2 induces acute lung injury and mortality in standard laboratory mice. Cell 2020;183(4):1070–85 e12.
[28] Huang C, Wang Y, Li X, Ren L, Zhao J, Hu Y, et al. Clinical features of patients infected with 2019 novel coronavirus in Wuhan, China. Lancet. 2020;395(10223):497–506.
[29] Benvenuto D, Angeletti S, Giovanetti M, Bianchi M, Pascarella S, Cauda R, et al. Evolutionary analysis of SARS-CoV-2: how mutation of Non-Structural Protein 6 (NSP6) could affect viral autophagy. J Infect 2020;81(1):e24–e7.
[30] Oostra M, Hagemeijer M, van Gent M, Bekker C, te Lintelo E, Rottier P, et al. Topology and membrane anchoring of the coronavirus replication complex: not all hydrophobic domains of nsp3 and nsp6 are membrane spanning. J Virol 2008;82(24):12392–405.
[31] Xia H, Cao Z, Xie X, Zhang X, Chen J, Wang H, et al. Evasion of Type I Interferon by SARS-CoV-2. Cell Reports 2020;33(1):108234.
[32] Forni D, Cagliani R, Clerici M, Sironi M. Molecular evolution of human coronavirus genomes. Trends Microbiol 2017;25(1):35–48.
[33] Angelini MM, Akhlaghpour M, Neuman BW, Buchmeier MJ. Severe acute respiratory syndrome coronavirus nonstructural proteins 3, 4, and 6 induce double-membrane vesicles. mBio 2013;4(4).
[34] Muramatsu T, Takemoto C, Kim YT, Wang H, Nishii W, Terada T, et al. SARS-CoV 3CL protease cleaves its C-terminal autoprocessing site by novel subsite cooperativity. Proc Natl Acad Sci USA. 2016;113(46):12997–3002.

[35] Kaushal N, Gupta Y, Goyal M, Khaiboullina SF, Baranwal M, Verma SC. Mutational frequencies of SARS-CoV-2 genome during the beginning months of the outbreak in USA. Pathogens 2020;9(7).
[36] Littler DR, Gully BS, Colson RN, Rossjohn J. Crystal structure of the SARS-CoV-2 non-structural protein 9, Nsp9. iScience. 2020;23(7):101258.
[37] Sutton G, Fry E, Carter L, Sainsbury S, Walter T, Nettleship J, et al. The nsp9 replicase protein of SARS-coronavirus, structure and functional insights. Structure 2004;12(2):341–53.
[38] Frieman M, Yount B, Agnihothram S, Page C, Donaldson E, Roberts A, et al. Molecular determinants of severe acute respiratory syndrome coronavirus pathogenesis and virulence in young and aged mouse models of human disease. J Virol 2012;86(2):884–97.
[39] Yuen CK, Lam JY, Wong WM, Mak LF, Wang X, Chu H, et al. SARS-CoV-2 nsp13, nsp14, nsp15 and orf6 function as potent interferon antagonists. Emerg Microbes Infect 2020;9(1):1418–28.
[40] Su YCF, Anderson DE, Young BE, Linster M, Zhu F, Jayakumar J, et al. Discovery and genomic characterization of a 382-nucleotide deletion in ORF7b and ORF8 during the early evolution of SARS-CoV-2. mBio 2020;11(4).
[41] Chiu RW, Chim SS, Tong YK, Fung KS, Chan PK, Zhao GP, et al. Tracing SARS-coronavirus variant with large genomic deletion. Emerg Infect Dis 2005;11(1):168–70.
[42] Lau SK, Feng Y, Chen H, Luk HK, Yang WH, Li KS, et al. Severe acute respiratory syndrome (SARS) Coronavirus ORF8 protein is acquired from SARS-related coronavirus from greater horseshoe bats through recombination. J Virol 2015;89(20):10532–47.
[43] Tang JW, Cheung JL, Chu IM, Sung JJ, Peiris M, Chan PK. The large 386-nt deletion in SARS-associated coronavirus: evidence for quasispecies? J Infect Dis 2006;194(6):808–13.
[44] Young BE, Fong SW, Chan YH, Mak TM, Ang LW, Anderson DE, et al. Effects of a major deletion in the SARS-CoV-2 genome on the severity of infection and the inflammatory response: an observational cohort study. Lancet 2020;396(10251):603–11.
[45] Dinnon K, Leist S, Schäfer A, Edwards C, Martinez D, Montgomery S, et al. A mouse-adapted model of SARS-CoV-2 to test COVID-19 countermeasures. Nature 2020;586(7830):560–6.
[46] Ge XY, Li JL, Yang XL, Chmura AA, Zhu G, Epstein JH, et al. Isolation and characterization of a bat SARS-like coronavirus that uses the ACE2 receptor. Nature 2013;503(7477):535–8.
[47] Chan J, Zhang A, Yuan S, Poon V, Chan C, Lee A, et al. Simulation of the clinical and pathological manifestations of coronavirus disease 2019 (COVID-19) in a golden syrian hamster model: implications for disease pathogenesis and transmissibility. Clin Infect Dis 2020;71(9):2428–46.
[48] McGowan D, Herschke F, Pauwels F, Stoops B, Last S, Pieters S, et al. Novel pyrimidine toll-like receptor 7 and 8 dual agonists to treat hepatitis B virus. J Med Chem 2016;59(17):7936–49.
[49] Hofmann H, Vanwalscappel B, Bloch N, Landau NR. TLR7/8 agonist induces a post-entry SAMHD1-independent block to HIV-1 infection of monocytes. Retrovirology 2016;13(1):83.
[50] Vanwalscappel B, Tada T, Landau NR. Toll-like receptor agonist R848 blocks Zika virus replication by inducing the antiviral protein viperin. Virology 2018;522:199–208.
[51] Zhao J, Wohlford-Lenane C, Zhao J, Fleming E, Lane TE, McCray Jr. PB, et al. Intranasal treatment with poly(I°C) protects aged mice from lethal respiratory virus infections. J Virol 2012;86(21):11416–24.
[52] Tian W, Zhang N, Jin R, Feng Y, Wang S, Gao S, et al. Immune suppression in the early stage of COVID-19 disease. Nat Commun 2020;11(1):5859.
[53] Sinha P, Matthay MA, Calfee CS. Is a "Cytokine Storm" Relevant to COVID-19? JAMA Intern Med 2020;180(9):1152–4.